

Reduced-Dimensional Whole-Body Control Based on Model Simplification for Bipedal Robots With Parallel Mechanisms

Yunpeng Liang[✉], Fulong Yin[✉], Zhen Li, Zhilin Xiong, Zhihui Peng, Yanzheng Zhao, and Weixin Yan[✉]

Abstract—The presence of parallel mechanisms in bipedal robots increases the complexity of modeling and control, making it crucial to manage the trade-off between model accuracy and real-time control. In this letter, we propose a reduced-dimensional whole-body controller for series-parallel bipedal robots, utilizing a floating-base multi-rigid body model with kinematic loops. Notably, we neglect the joint acceleration and closed-loop acceleration constraints of the parallel mechanisms, reducing the dimensionality of variables and constraints in the whole-body optimization problem while ensuring compliance with actuated joint torque limits. Quantitative experiments indicate that, compared to the complete series-parallel model, the impact of inertial forces resulting from the parallel joint acceleration is negligible. Additionally, physical locomotion and disturbance tests demonstrate that our proposed controller can enhance computational efficiency by over 20%, with comparable locomotion performance and disturbance rejection ability.

Index Terms—Humanoid and bipedal locomotion, whole-body motion planning and control, series-parallel mechanisms.

I. INTRODUCTION

PARALLEL mechanisms (PM) are commonly integrated into wheeled [1] and biped [2], [3], [4] robots as modular subsystem units due to their superior stiffness, optimal payload-to-weight ratio, and dynamic characteristics [5]. These mechanisms introduce additional linkages and joints to achieve specific degrees of freedom (DOFs). For instance, our bipedal robot incorporates the 2RSS-1 U mechanism [6], which facilitates ankle pitch and roll DOFs, as illustrated in Fig. 1.

Over the past two decades, Whole-body control (WBC) has been the predominant approach for underactuated robots like bipeds [7], quadrupeds [8], and wheeled [9] robots. It effectively addresses multiple tasks such as achieving target poses and wrenches while handling constraints like floating-base dynamics, contact, and actuator limits. Since its initial application [10]

Received 25 August 2024; accepted 27 December 2024. Date of publication 1 January 2025; date of current version 10 January 2025. This article was recommended for publication by Associate Editor M. Tucker and Editor A. Kheddar upon evaluation of the reviewers' comments. This work was supported by AgiBot Technology Company Ltd. (*Corresponding author:* Weixin Yan.)

Yunpeng Liang, Yanzheng Zhao, and Weixin Yan are with the School of Mechanical Engineering, Shanghai Jiao Tong University, Shanghai 200240, China (e-mail: lyppp597@sjtu.edu.cn; xiaogu4524@sjtu.edu.cn; yzh-zhao@sjtu.edu.cn).

Fulong Yin, Zhen Li, Zhilin Xiong, and Zhihui Peng are with the AgiBot Technology Company Ltd., Shanghai 200120, China (e-mail: yinfulong@zhiyuan-robot.com; lizhen@zhiyuan-robot.com; xiongzhilin@zhiyuan-robot.com; pengzhihui@zhiyuan-robot.com).

This letter has supplementary downloadable material available at <https://doi.org/10.1109/LRA.2024.3524902>, provided by the authors.

Digital Object Identifier 10.1109/LRA.2024.3524902

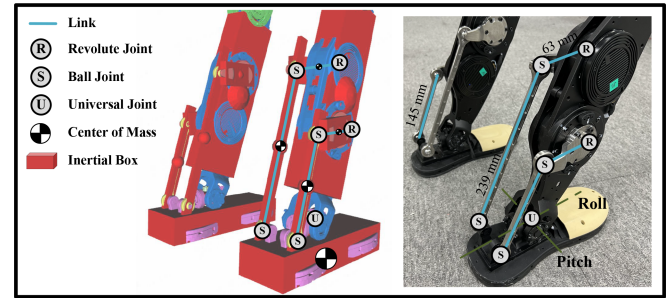


Fig. 1. Our robot features an ankle parallel mechanism. The mass and inertia of the connecting rod are negligible compared to those of the foot sole.

to humanoid robots, WBC has evolved into two primary classes: those based on the closed-form nullspace projection [11], [12] and those relying on the quadratic programming (QP) [13], [14], [15]. While these methods are well-established for serial models, they face significant limitations when applied to the system with PM. The serial WBC produces less accurate solutions because it fails to capture the correct dynamics of the system and cannot enforce physical constraints through serial box constraints [5]. Incorporating the modeling of PM into WBC can address these drawbacks, but the inherent nonlinearity and multivariable coupling in series-parallel robots, driven by closed-loop chains and multidimensional motions, present a significant challenge for implementation in real-time dynamic control. Therefore, achieving a trade-off between modeling accuracy and computational efficiency is crucial.

A straightforward method involves decoupling the serial and parallel modules to avoid complex modeling and achieve efficient parallel computation. The actuated torques can be calculated through the serial WBC and the parallel Jacobian matrix [16], but this method inherits the limitations of the serial WBC. The WBC method that incorporates complete dynamics has been studied by several researchers [5], [17], [18]. An approach based on the space projection [19] has been conducted on the RH5 robot [5], which maps all joint variables to the actuator space, eliminating the closed-loop constraint forces in the equations of motion (EoM). Although this method is computationally efficient, its applicability is limited due to the complexity or the absence of the analytical expression for deriving explicit closed-loop constraints. The general approach integrating the implicit closed-loop constraints into WBC has been applied in robots such as Digit [18] and Kangaroo [20]. In these implementations, all joint variables are introduced and the closed-loop constraints

at the acceleration level are formulated as equality constraints. Although the complete dynamics of the series-parallel model are considered, the increased computational burden due to the additional joints and constraints has not been extensively discussed, and some of their work is validated only through simulations. There is still a need to simplify the model complexity and reduce computational overhead, especially for control systems with high real-time requirements.

Model simplification has proven effective for inverse dynamics control of robots with PM, either by neglecting some bodies [21], [22], [23] or by omitting complicated dynamics terms [24]. Kumar et al. [23] studied the errors from the neglected dynamics based on the various simplified models, indicating that neglecting the dynamics of certain sub-mechanisms can decrease the calculation time without resulting in significant errors. However, their experiments were limited to single-leg up-down movements, without involving dynamic walking scenarios. Roig et al. [4] developed a reduced model on a 76-DOF humanoid robot, retaining parallel joints and closed-loop constraint forces in specific kinematic loops to enhance calculation efficiency. However, parallel-actuated torques in the unmodeled kinematic loops cannot be directly accounted for. The research based on model simplification for serial-parallel biped robots is still challenged due to the inherent complexity arising from high dimensionality and underactuation.

To address the limitations of the serial WBC and find a trade-off between the model accuracy and real-time control, we present a reduced-dimensional whole-body control (RD-WBC) method based on the model simplification strategy, whose validity for our bipedal robots is evaluated in Section V. Compared to the existing methods in [17], [18], we introduce only closed-loop constraint forces, thereby reducing the dimensionality of the variables and constraints in the QP optimization. Our main contributions are:

- We present a model simplification strategy to balance model accuracy and real-time control by neglecting PM's joint acceleration and the close-loop acceleration constraints in the dynamics equation. (Section III).
- We propose a reduced-dimensional whole-body controller for series-parallel bipedal robots, designed to lower the complexity of the QP problem while directly considering actuated torque limits. (Section IV).
- Physical experiments demonstrate that RD-WBC enhances computational efficiency while achieving effective dynamic locomotion performance and disturbance rejection capability, with minimal compromise to the model accuracy. (Section V).

II. CLOSED-LOOP CHAIN KINEMATICS

In this section, we derive the closed-loop constraints of PM and introduce several kinematic solvers. We use the fixed-base model as an example, noting that all formulas can be easily extended to the floating-base model since the floating base does not affect the closed-loop chains.

A. Model

The spanning tree graph (\mathcal{T}) can describe the serial structure of robots, providing a single unique path between any two nodes [19]. The spanning tree for our robot's leg is shown in

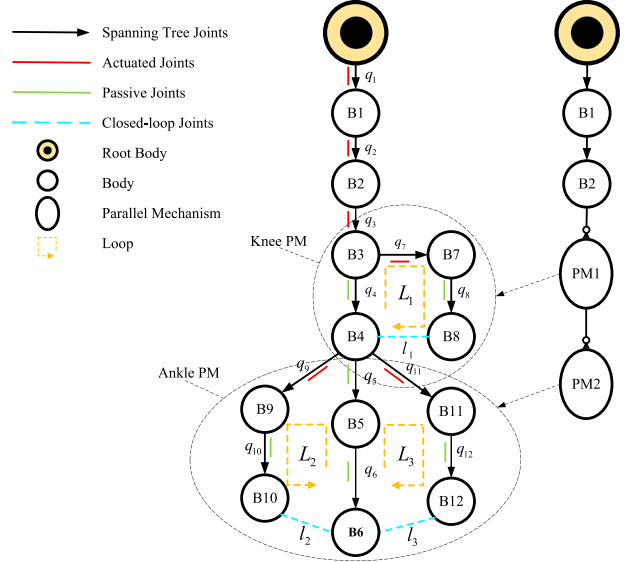


Fig. 2. The spanning tree graph \mathcal{T} of our robot's single leg.

Fig. 2, where all the revolute joints are categorized as follows: actuated joints directly powered by motors, passive joints without motor actuation, and closed-loop joints located at connections between different branches in PM, as marked in Fig. 2. There are three kinematic loops in the spanning tree, the first loop L_1 is related to the knee joint, which can be treated as the actuated joint due to the particularity of the parallelogram mechanism [25]. The second loop L_2 and third loop L_3 involve the ankle joints, which consist of 2 actuated joints, 4 passive joints (pitch, roll, and ball joints), and 2 closed-loop joints.

B. Loop Constraint Equations

1) *Geometric Constraint*: A coordinate transformation exists from the predecessor to the successor of the closed-loop joint, which equates to the joint transformation. The geometric constraints can be denoted as:

$${}^s \mathbf{X}_p(\mathbf{q}) = {}^s \mathbf{X}_0(\mathbf{q}) ({}^p \mathbf{X}_0(\mathbf{q}))^{-1} = \mathbf{X}(\mathbf{q}_{l_k}) \quad (1)$$

where ${}^s \mathbf{X}_p \in SE(3)$ denotes the homogeneous transformation from the frame of predecessor p to the frame of successor s , of the k th closed-loop joint l_k . This transformation comprises the translation $\mathbf{p} \in \mathbb{R}^3$ and the rotation $\mathbf{E} \in SO(3)$. The right subscript 0 denotes w.r.t the inertial frame. The generalized coordinates $\mathbf{q} \in \mathbb{R}^{n_j}$ consist of all joint coordinates. We omit the direct dependence on the generalized coordinates \mathbf{q} and the closed-loop joint coordinates $\mathbf{q}_{l_k} \in \mathbb{R}^7$ for the brevity of notation.

(1) corresponds to both rotation and translation:

$$\phi_{l_k}(\mathbf{q}) := \begin{cases} \log SO_3(({}^s \mathbf{E})^T \mathbf{E}_{l_k} ({}^p \mathbf{E})) & = \mathbf{0}_{3 \times 1} \\ ({}^p \mathbf{E})^T ({}^s \mathbf{p} - {}^p \mathbf{p}) - \mathbf{p}_{l_k} & = \mathbf{0}_{3 \times 1} \end{cases} \quad (2)$$

In (2), we only consider the rows corresponding to the constraint-force subspace [19] \mathbf{T}_{l_k} and the other rows in the motion subspace \mathbf{S}_{l_k} always equate to zero. All the closed-loop geometric constraints in the spanning tree can be denoted as $\phi_l(\mathbf{q}) = \mathbf{0}_{m \times 1}$.

2) *Velocity Constraint*: The velocity of the closed-loop joint $\mathbf{v}_{l_k} \in \mathbb{R}^6$ is constrained to be zero in the constraint-force subspace \mathbf{T}_{l_k} .

$$\mathbf{T}_{l_k}^T \mathbf{v}_{l_k} = \underbrace{\mathbf{T}_{l_k}^T \text{Adj}^T(p \mathbf{X}) ({}^s \mathbf{J} - {}^p \mathbf{J})}_{:= \mathbf{J}_{l_k}} \mathbf{v} = 0 \quad (3)$$

where

$$\text{Adj}^T(p \mathbf{X}) = \begin{bmatrix} {}^p \mathbf{E} & [{}^{sp} \mathbf{p}] \times {}^p \mathbf{E} \\ \mathbf{0}_{3 \times 3} & {}^p \mathbf{E} \end{bmatrix}_{6 \times 6}^T \quad (4)$$

is the adjoint transformation of a homogeneous transform matrix. The translation between p, s is denoted as ${}^{sp} \mathbf{p}$ and $[\cdot] \times$ is used for the skew-symmetric cross-product matrix of a vector. The generalized velocity is denoted as $\mathbf{v} \in \mathbb{R}^{n_j}$.

3) *Acceleration Constraint*: The acceleration of closed-loop joints $\dot{\mathbf{v}}_{l_k}$ in the constraint-force subspace $\mathbf{T}_{l_k}^T$ satisfies the following equation [19].

$$\mathbf{T}_{l_k}^T \dot{\mathbf{v}}_{l_k} = \mathbf{T}_{l_k}^T ({}^p \mathbf{v} \times \mathbf{v}_{l_k}) \quad (5)$$

Expanding $\dot{\mathbf{v}}_{l_k}$ using the Jacobian matrices, we get:

$$\mathbf{J}_{l_k} \dot{\mathbf{v}} = \mathbf{T}_{l_k}^T ({}^p \mathbf{v} \times \mathbf{v}_{l_k}) - \mathbf{T}_{l_k}^T \text{Adj}^T(p \mathbf{X}) ({}^s \mathbf{J} - {}^p \mathbf{J}) \mathbf{v} \quad (6)$$

where $\dot{\mathbf{v}} \in \mathbb{R}^{n_j}$ denotes the generalized acceleration.

C. Closed-Loop Kinematics Solvers

We designed kinematics solvers to calculate PM's joint positions, velocities, and accelerations based on the implicit constraint equations in Section II-B, which are useful to update the information of the passive joints in the state estimation module and calculate the information of the actuated joints in the series-parallel inverse kinematic (SPIK) module. The forward kinematics (FK) problem involves computing the passive joint information $(\mathbf{q}_p, \mathbf{v}_p, \dot{\mathbf{v}}_p)$ given a reference for the actuated joints $(\mathbf{q}_a, \mathbf{v}_a, \dot{\mathbf{v}}_a)$. The inverse kinematics problem is exactly the opposite of it. For simplicity, the following details use the FK problem as an example.

The structure of the position QP problem is as follows:

$$\begin{aligned} \underset{\delta \mathbf{q}}{\text{argmin}} & \| \phi_l(\mathbf{q}) + \mathbf{J}_l(\mathbf{q}) \delta \mathbf{q} \| \\ \text{s.t. } & \underline{\mathbf{q}}_p \leq \mathbf{q}_p + \delta \mathbf{q}_p \leq \bar{\mathbf{q}}_p \end{aligned} \quad (7)$$

where \mathbf{J}_l can be obtained by collecting the equations (3) of all the closed-loop joints together. We use the right subscripts a, p to denote the information of the actuated and passive joints respectively, and notations $\underline{\cdot}$ and $\bar{\cdot}$ denote a vector's lower and upper bounds.

Given the positions of the actuated joints \mathbf{q}_a , we can solve the QP problem (7) t iterations and update $\mathbf{q}^{[t]}$ as $\mathbf{q}^{[t]} = \mathbf{q}^{[t-1]} + \delta \mathbf{q}^{[t]}$ until the geometric error $\phi_l(\mathbf{q}^{[t]})$ falls below the specified threshold.

The structure of the velocity QP problem is as follows:

$$\begin{aligned} \underset{\mathbf{v}_p}{\text{argmin}} & \| \mathbf{J}_{la}(\mathbf{q}) \mathbf{v}_a + \mathbf{J}_{lp}(\mathbf{q}) \mathbf{v}_p \| \\ \text{s.t. } & \underline{\mathbf{v}}_p \leq \mathbf{v}_p \leq \bar{\mathbf{v}}_p \end{aligned} \quad (8)$$

where $\mathbf{J}_{la}(\mathbf{q})$ and $\mathbf{J}_{lp}(\mathbf{q})$ correspond to the Jacobians of the actuated and passive joints, respectively.

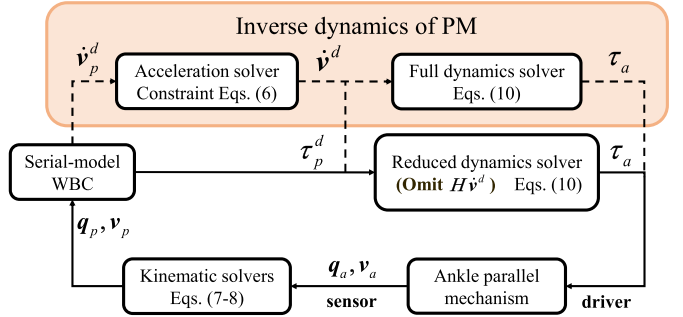


Fig. 3. Decoupled model control (DMC) block diagram. The desired acceleration input to the full dynamics solver must satisfy the closed-loop acceleration constraints, which are omitted in the simplified dynamics solver.

Given the velocities of the actuated joints \mathbf{v}_a , the velocities of the passive joints \mathbf{v}_p can be determined by solving the QP problem (8) once. To avoid redundancy, the details of the acceleration QP problem are omitted. It suffices to state that (6) is used as the objective function to be minimized.

III. PRINCIPLE OF MODEL SIMPLIFICATION

In this section, we outline the primary principle behind the model simplification strategy and provide the error analysis resulting from it, which underpins the RD-WBC method.

A. Appropriate Assumptions

The introduction of PM in the series-parallel model increases the complexity of QP, primarily by increasing the dimensions of both optimization variables and equality constraints. Since the QP-based inverse dynamics controller mainly focuses on joint accelerations and their related constraints, neglecting the inertial forces caused by them can substantially simplify the QP problem. Given that the inertia of the connecting rods in PM is typically small compared to other links [18], we assume zero parallel joint accelerations in PM, rendering the acceleration-level constraints (6) insignificant. This assumption forms the foundation of our model simplification approach.

B. Model Simplification Error Analysis

We evaluate the error of the simplified model by considering the series-parallel torque conversion problem, where the EoM of PM can be expressed as:

$$\mathbf{H} \dot{\mathbf{v}} + \mathbf{C} + \mathbf{g} = \boldsymbol{\tau} + \mathbf{J}_l^T \boldsymbol{\lambda}_l \quad (9)$$

where \mathbf{H} , \mathbf{C} , \mathbf{g} , $\boldsymbol{\lambda}_l$, and $\boldsymbol{\tau}$ denote inertia matrix, Coriolis and centrifugal terms, gravity term, closed-loop constraint forces, and generalized forces respectively.

Given the desired passive joint torques τ_p^d and accelerations $\dot{\mathbf{v}}_p^d$ from the serial WBC, as shown in Fig. 3, the actuated joint torques τ_a can be calculated by the acceleration and the full dynamics solvers. However, if we assume the zero accelerations of PM, the actuated joint torques τ_a can be calculated using the simplified dynamics solver. The torque differences between the two strategies can be defined as the errors introduced by our assumptions, which effectively disregard the influence of inertial forces.

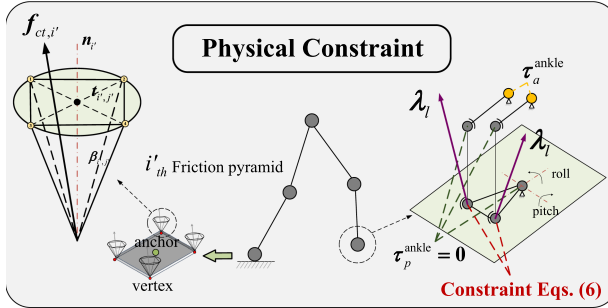


Fig. 4. This graph illustrates the friction cone constraint (left) and loop closure constraint (right). The actuated and passive joint torque relationship is enforced by the closed-loop constraint forces λ_l .

The structure of the QP problem with full dynamics is:

$$\underset{\lambda_l, \tau_a}{\text{argmin}} \left\| \begin{bmatrix} \mathbf{J}_{la}^T & \mathbf{I} \\ \mathbf{J}_{lp}^T & \mathbf{0} \end{bmatrix} \begin{bmatrix} \lambda_l \\ \tau_a \end{bmatrix} - \begin{bmatrix} \Pi_{a,v}(\mathbf{H}\dot{\mathbf{v}}^d + \mathbf{C} + \mathbf{g}) \\ \tau_p^d + \Pi_{p,v}(\mathbf{H}\dot{\mathbf{v}}^d + \mathbf{C} + \mathbf{g}) \end{bmatrix} \right\| \\ \text{s.t. } \underline{\tau}_a \leq \tau_a \leq \bar{\tau}_a \quad (10)$$

where the selection matrices $\Pi_{a,v}$ and $\Pi_{p,v}$ are used to decompose the EoM in the spanning tree space into the actuated and passive joint spaces.

The upper part of (10) relates the forces λ_l to the actuated joint torque τ_a , while the lower part constrains the passive joint torques τ_p^d , covering the desired torques in the serial WBC (e.g., ankle pitch and roll) and undrivable zero torques (e.g., ball joints). The relationship between actuated and passive joint torques is established through closed-loop forces. If the inertial forces $\mathbf{H}\dot{\mathbf{v}}^d = 0$ in (10), the QP problem with full dynamics simplifies to its reduced version.

IV. FULL AND REDUCED-DIMENSIONAL WHOLE-BODY CONTROL

The full-dimensional WBC (FD-WBC) described in [18], [20] incorporates all joint variables and includes closed-loop constraints at the acceleration level. In this section, we apply the assumption from Section III-A to the WBC optimization of the series-parallel model, leading to the development of a reduced-dimensional whole-body controller. The overview of our control framework is shown in Fig. 5.

A. Hierarchical Quadratic Programming

RD-WBC calculates the feedforward torques accounting for the physical constraints and task objectives. The problem can be solved using a weighted QP [14] or a hierarchical QP. To ensure the integration of solutions for lower-priority tasks into the outcomes of higher-priority ones, we address optimal variables through the HQP formulation described in [26].

$$\underset{\mathbf{z}_{i+1}, \mathbf{r}_{i+1}}{\text{argmin}} \|\mathbf{A}_{i+1}(\xi^* + \mathbf{N}_i \mathbf{z}_{i+1}) - \mathbf{b}_{i+1}\| + \|\mathbf{r}_{i+1}\|$$

$$\text{s.t. } \mathbf{L} = \begin{cases} \mathbf{h}_j \leq D_j(\xi^* + \mathbf{N}_i \mathbf{z}_{i+1}) + \mathbf{r}_j^* \leq \bar{\mathbf{h}}_j & \text{for } j \in \{0, 1, \dots, i\} \\ \mathbf{h}_{i+1} \leq D_{i+1}(\xi^* + \mathbf{N}_i \mathbf{z}_{i+1}) + \mathbf{r}_{i+1} \leq \bar{\mathbf{h}}_{i+1} \end{cases} \quad (11)$$

TABLE I
THE PRIORITIZED TASKS USED IN FD-WBC AND RD-WBC

Priority	Task
0	Overall floating-base equations of motion
	Torque limits and friction cone
	Non-slipping constraint of the contact leg
	Close-loop acceleration constraint (optional)
1	Zero torque constraint of the passive joints
	Body linear and angular motion tracking
2	Swing leg motion tracking
	Contact force tracking
	Closed-loop constraint force minimization

where \mathbf{A}, \mathbf{b} and \mathbf{D}, \mathbf{h} are formed by the equality constraints and the inequality constraints \mathbf{L} . The optimal solution ξ^* is determined by i tasks. The slack variables \mathbf{r}_j^* satisfy tasks of the j th layer and remain constant in the subsequent optimization. The i th layer's statically consistent nullspace is denoted as $\mathbf{N}_i = \mathcal{N}([\mathbf{A}_1^T, \dots, \mathbf{A}_i^T]^T)$ and the vector \mathbf{z}_{i+1} lives in the row space of the \mathbf{N}_i .

B. Prioritized Constraints and Tasks

We first introduce the FD-WBC method, where the optimization variables can be selected as $\xi_{\text{opt}} = [\dot{\mathbf{v}}, \lambda]^T$, where $\dot{\mathbf{v}} \in \mathbb{R}^{6+n_j}$ denotes the accelerations of the floating base and spanning tree joints. The constraint forces $\lambda = [\lambda_l, \lambda_c]^T$ consist of the internal and external constraint forces. The highlighted tasks in Table I are specifically tailored for PM using FD-WBC or RD-WBC methods, and the following sections describe each task from highest to lowest priority.

1) *Floating-Base Dynamics Constraint*: Utilizing orthogonal decomposition [28], the overall EoM incorporating the floating base, external contact, and internal constraints can be simplified as six equations related to the floating base.

$$\mathbf{\Pi}_b(\mathbf{H}\dot{\mathbf{v}} + \mathbf{C} + \mathbf{g}) = \mathbf{\Pi}_b \left(\mathbf{S}^T \boldsymbol{\tau} + [\mathbf{J}_l^T \quad \mathbf{J}_c^T] \begin{bmatrix} \lambda_l \\ \lambda_c \end{bmatrix} \right) \quad (12)$$

where $\mathbf{\Pi}_b = [\mathbf{I}_{6 \times 6}, \mathbf{0}_{6 \times n_j}]$ and $\mathbf{S} = [\mathbf{0}_{n_j \times 6}, \mathbf{I}_{n_j \times n_j}]$ are selection matrices associated with the floating base and spanning tree joints, respectively. The contact Jacobian matrix \mathbf{J}_c pertains to external contacts.

The closed-loop constraints exclusively impact the joints within the loops, thus remaining unaffected by the presence of the closed-loop joints. (12) can be rewritten as

$$[\mathbf{\Pi}_b \mathbf{H} \quad \mathbf{0}_{6 \times m} \quad -\mathbf{\Pi}_b \mathbf{J}_c^T] \begin{bmatrix} \dot{\mathbf{v}} \\ \lambda \end{bmatrix} = -\mathbf{\Pi}_b(\mathbf{C} + \mathbf{g}) \quad (13)$$

2) *Loop Closure Constraint*: There exist two points that need to be considered. One is the closed-loop acceleration constraints represented in (6). The complete series-parallel model must satisfy these acceleration constraints [18], [20].

The other is to constrain the torques of passive joints to be zero represented in Fig. 4, which is determined by physical constraints and can be interpreted as the intention of the lower part of (10). It can be formed as:

$$\mathbf{\Pi}_{p,v}(\mathbf{H}\dot{\mathbf{v}} + \mathbf{C} + \mathbf{g} - [\mathbf{J}_l^T \quad \mathbf{J}_c^T] \boldsymbol{\lambda}) = \mathbf{0} \quad (14)$$

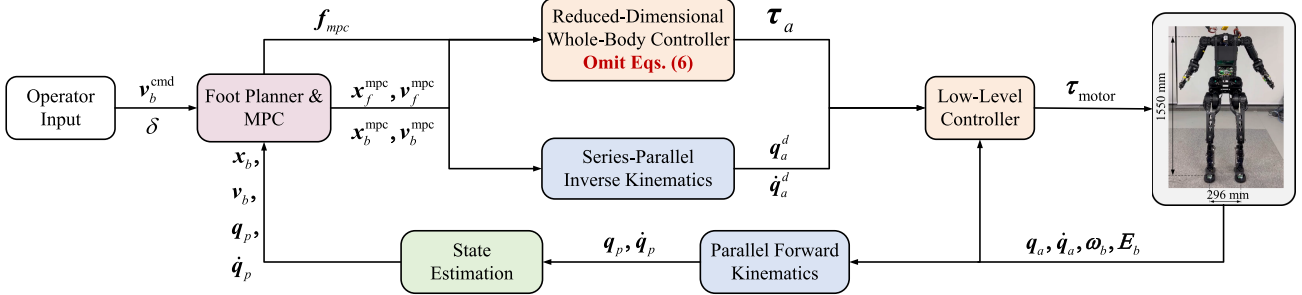


Fig. 5. The overview of our control framework. Utilizing the user-commanded gait type δ and speed v_b^{cmd} , the non-linear model predictive control (MPC) [27] based on the centroidal dynamics computes desired contact forces and foot/body motion trajectory. From these, the RD-WBC module computes joint torques, and the SPIK module calculates the joint positions and velocities, which are then transmitted to a low-level controller.

3) *Friction Cone Constraint:* For flat, polygonal contact surfaces subjected to distributed loading, an equivalent representation can be achieved by employing point contacts at the vertices. We approximate the friction cone using a friction pyramid [20] with 4 edges at each vertex. The lumped contact force $f_{ct,i'}$ at the i'_{th} vertex can be represented as:

$$\begin{aligned} f_{ct,i'} = \sum_{j'=1}^4 \lambda_{i',j'} \beta_{i',j'} &= \sum_{j'=1}^4 \lambda_{i',j'} (\mathbf{n}_{i'} + \mu \mathbf{t}_{i',j'}) \\ \text{s.t. } 0 \leq \lambda_{i',j'} \leq \bar{\lambda}_{i',j'} \end{aligned} \quad (15)$$

where $\beta_{i',j'}$ denotes the basis vector of the friction pyramid, which is composed of the normal vector $\mathbf{n}_{i'}$ and tangent vector $\mathbf{t}_{i',j'}$ shown in Fig. 4, with a static friction coefficient $\mu = 0.6$. The non-negative coordinate vector of the i'_{th} friction pyramid is denoted as $\boldsymbol{\lambda}_{i'} = [\lambda_{i',1}, \dots, \lambda_{i',4}]^T$.

4) Torque Bounds Constraint:

$$\tau_a \leq \Pi_{a,v}(\mathbf{H}\dot{\mathbf{v}} + \mathbf{C} + \mathbf{g} - [\mathbf{J}_l^T \quad \mathbf{J}_c^T]\boldsymbol{\lambda}) \leq \bar{\tau}_a \quad (16)$$

5) *Non-Slipping Constraint:* By contact constraints, there is no motion observed w.r.t the inertial frame. Calling \mathbf{x}_c the positions and orientations of the external contact points, we will have:

$$\ddot{\mathbf{x}}_c = \dot{\mathbf{J}}_c \mathbf{v} + \mathbf{J}_c \dot{\mathbf{v}} = \mathbf{0} \quad (17)$$

6) *Body and Foot Motion Tasks:* For the body's linear and angular motion task, we utilize the PD law to calculate the desired accelerations $\ddot{\mathbf{p}}_b$ and $\dot{\mathbf{w}}_b$ as:

$$\begin{aligned} \begin{bmatrix} \ddot{\mathbf{p}}_b \\ \dot{\mathbf{w}}_b \end{bmatrix} &= \begin{bmatrix} \mathbf{K}_{p,p}(\mathbf{p}_b^{\text{mpc}} - \mathbf{p}_b) + \mathbf{K}_{d,p}(\dot{\mathbf{p}}_b^{\text{mpc}} - \dot{\mathbf{p}}_b) \\ \mathbf{K}_{p,\omega} \log_{SO3}(\mathbf{E}_b \mathbf{E}_b^{\text{mpc}T}) + \mathbf{K}_{d,\omega}(\omega_b^{\text{mpc}} - \omega_b) \end{bmatrix} \\ &= \mathbf{J}_b \dot{\mathbf{v}} + \dot{\mathbf{J}}_b \mathbf{v} \end{aligned} \quad (18)$$

where $\mathbf{K}_{p,p(\omega)}$ and $\mathbf{K}_{d,p(\omega)}$ are diagonal matrices of positive PD gains, namely stiffness and damping. The script mpc stands for the reference from MPC and b denotes the body's information.

The swing foot motion task is similar to the body motion task, which will not be elaborated upon here.

7) *Contact Forces Task:* For the task of the foot contact wrench, the lumped force $f_{ct,i'}$ in (15) can be expressed in matrix multiplication form using the basic matrix $\mathbf{E}_{i'}^{\text{bas}} = [\beta_{i',1}, \dots,$

$\dots, \beta_{i',4}]^T$ and the non-negative coordinate vector $\boldsymbol{\lambda}_{i'}$.

$$\sum_{i'=1}^4 \left[[\mathbf{p}_{i'}^{\text{ver}} - \mathbf{p}^{\text{anc}}] \times \mathbf{E}_{i'}^{\text{bas}} \right] \boldsymbol{\lambda}_{i'} = \mathbf{f}^{\text{mpc}} \quad (19)$$

where $\mathbf{p}_{i'}^{\text{ver}}$ and \mathbf{p}^{anc} denote the position of the i'_{th} vertex and the anchor, respectively.

8) *Minimal Closed-Loop Constraint Forces:* This normalization term reduces the force impact at the closed-loop connection point and lowers drive power consumption.

After finding the optimal solution $\xi_{\text{opt}}^* = [\dot{\mathbf{v}}^*, \boldsymbol{\lambda}^*]^T$, the forward torques τ^* can be calculated by (12).

C. Implementation of RD-WBC

Applying the assumption from Section III-A results in two changes to the whole-body optimization problem:

- The number of optimization variables in the QP problem is reduced, with $\xi_{\text{opt}} = [\dot{\mathbf{v}}, \boldsymbol{\lambda}]^T = [\dot{\mathbf{v}}_{bs}, \mathbf{0}_{n_j-n_s}, \boldsymbol{\lambda}]^T$, where $\dot{\mathbf{v}}_{bs} \in \mathbb{R}^{6+n_s}$ denotes the accelerations of the floating base and serial joints. The parallel joint accelerations are consistently set as $\mathbf{0}_{n_j-n_s}$.
- The dimension of equality constraints in the QP problem is decreased. The closed-loop joint acceleration constraint (6) no longer needs to be strictly enforced.

V. EXPERIMENTAL RESULTS

To validate the assumption of the simplified model and demonstrate the benefits and effectiveness of RD-WBC, this section presents experiments conducted in *Mujoco* [29] and on our physical robot, *Raise-A2*, which stands 1.55 m tall, weighs 60 kg, and features 32 DoFs (14 in two arms and 12 in two legs) as shown on the rightmost side of Fig. 5.

A. Setup

We use *Eigen* [30] as a linear algebra library. For modeling and computation of kinematics and dynamics, we expand the open-source multi-rigid body dynamics library *pinocchio* [31] using the formulations derived in Section II-B. To solve the QP problems, we use a custom open-source solver *qpOASES* [32]. Primary control signals are generated in a 1 kHz control loop which runs on a dedicated on-board computer¹ together with

¹A ubuntu22.04 with 2.9 GHz dual-core Intel Core i7-1195G7 processor.

TABLE II
DIFFERENT GAIT PARAMETERS

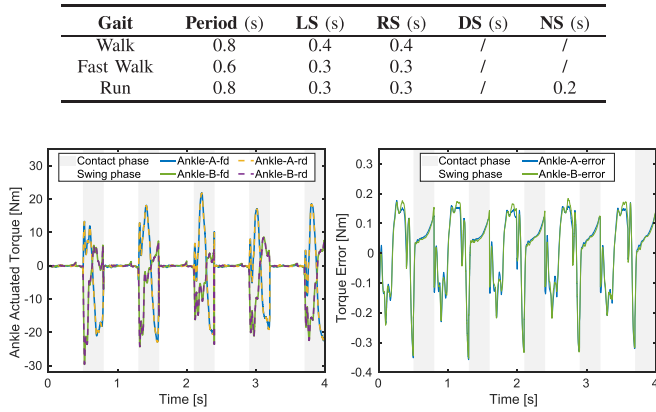


Fig. 6. The comparison of the ankle joint torques based on the complete and simplified models in the running gait.

TABLE III
THE TORQUE AND POWER ERROR METRICS DURING VARIOUS GAITS

Gait	Simulation		Physical Robot	
	NTPE ($\frac{\Delta \tau}{\tau_{\text{RMS}}} \%$)	CPE ($\frac{\Delta P}{P} \%$)	NTPE	CPE
Walk	0.77	2.89	1.05	3.91
Fast Walk	0.98	3.21	1.45	4.67
Run	1.53	2.81	1.90	4.40

MPC and WBC, and we adopt the method proposed in [33] to achieve the state estimation.

B. Experiments

1) *Simplified Model Validation*: To determine whether the influence of the inertial forces of PM can be omitted, we evaluate the actuated torque error at different gaits: walk, fast walk, and run. The gaits periods, left support (LS), right support (RS), double support (DS), and none support (NS) periods are listed in Table II.

The error evaluation between the reduced and full dynamics models is shown in Fig. 6. The torque error is calculated based on the error analysis introduced in Section III-B. In the support phase, the torque error is minimal compared to the actuated torque due to the influence of ground contact forces and the non-slip constraint. In the swing phase, the torque error slightly increases due to tracking the leg swing task but is effectively compensated by the joint PD control.

Following the power error metric outlined in [23], we calculate the cumulative power percent error (CPE) and the normalized torque percent error (NTPE) using the root mean square (RMS) over four gait cycles, as listed in Table III. For the run gait, CPE and NTPE remain within 4.4% and 1.9%, respectively. This indicates that neglecting the closed-loop acceleration constraint and the inertial force, resulting from the parallel joint acceleration, has a negligible effect on the overall system dynamics.

2) *Torque Safeguarding*: We apply external perturbations to the robot during locomotion to demonstrate the necessity of actuated torque constraints. Specifically, a 2 kg ball with a forward velocity of 5 m/s is released from the sagittal or coronal planes in simulation.

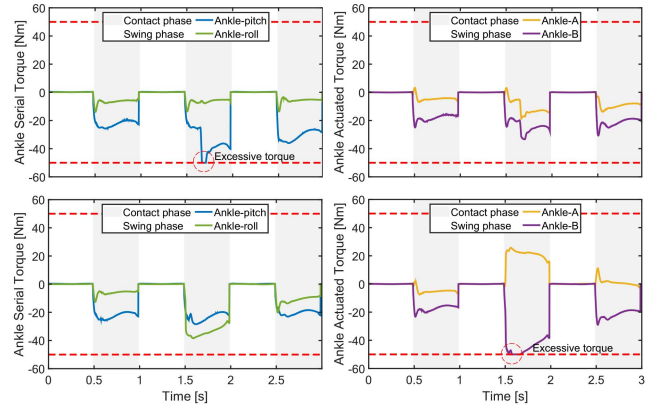


Fig. 7. The changes of the serial and actuated torques by DMC. Top row: sagittal plane perturbation. Bottom row: coronal plane perturbation.

Fig. 7 highlights two issues with DMC: one with pre-limited actuated torques (top) and one without timely limitation (bottom). When sagittal plane perturbations occur, the ankle-pitch joint torque reaches its limit first, though significant margins remain for other actuated joints, showing that maximum actuation torques are underutilized. Conversely, with coronal plane perturbations, the ankle-B joint torque is hardware-limited, but the desired serial WBC torques stay within reasonable bounds. Thus, DMC fails to ensure torque safety and optimal hardware performance as it only constrains serial joint torques. By contrast, RD-WBC and FD-WBC introduce the closed-loop constraint forces, directly limiting actuated joints as described in (16). However, due to the assumption in Section III-A, RD-WBC cannot directly enforce acceleration limits on actuated joints. FD-WBC can incorporate these limits but at the expense of a higher computational load.

3) *Locomotion Performance and CPU Consumption*: To demonstrate the locomotion performance and computational advantages of RD-WBC, we compare it with FD-WBC proposed in [17], [20] during dynamic locomotion. In the simulation, the robot accelerates from rest to 1.6 m/s, undergoing three gait transitions listed in Table II. In physical experiments, it accelerates to 0.9 m/s with two gait transitions, excluding the running gait. However, the running gait is tested separately at a velocity of 0.5 m/s.

The trajectory tracking results achieved by RD-WBC are illustrated in Fig. 8. We use the root mean square error (RMSE) and the population standard deviation (PSD) metrics to evaluate the tracking performance of both methods on the robot's behavior. In the simulation, the robot is tested under identical commands and conditions. Although the RMSE ratios for expected motion behaviors, such as forward body velocity v_x , lateral body position p_y , body height p_z , and pitch angle θ exceed 1, implying that RD-WBC introduces slightly larger tracking errors, they remain close to 1 as shown in Table IV. The PSD of the actual behavior reflects the body fluctuations, with both controllers achieving comparable results for the body pitch angle and height. In physical experiments, although we conduct three tests for each controller, ensuring identical experimental conditions is challenging due to inherent uncertainties (e.g., ground parameters and state estimation). As shown in Table IV, the RMSE ratio of the forward body velocity is less than 1, demonstrating

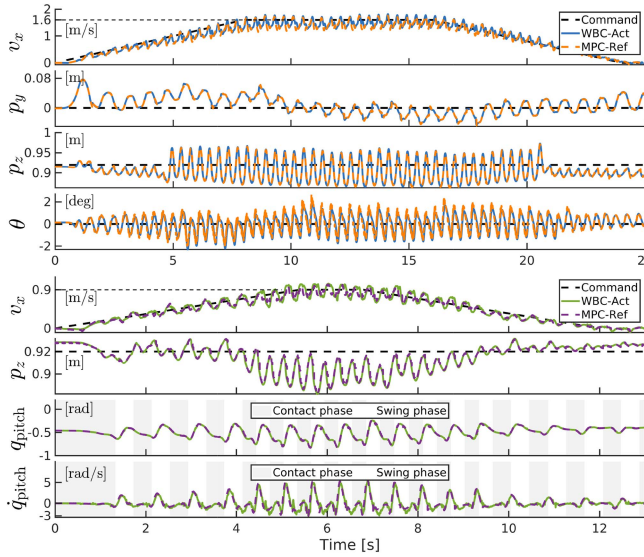


Fig. 8. Tracking results of the body task and the ankle joint trajectory using RD-WBC during dynamic locomotion. Top row: simulated experiment (running). Bottom row: physical experiment (fast walking).

TABLE IV
COMPARISON OF TRACKING ERROR BETWEEN [17] AND OUR METHOD

Environment	Behavior	RMSE Ratio (RD-WBC / FD-WBC)	PSD
Mujoco (Run)	Forward Velocity (m/s)	1.016	0.5303 / 0.5371
	Lateral Position (m)	1.024	0.0312 / 0.0236
	Body Height (m)	1.027	0.0258 / 0.0255
	Body Pitch (deg)	1.019	0.6433 / 0.5887
Physical World (Fast Walk)	Forward Velocity (m/s)	0.982	0.3184 / 0.3202
	Body Height (m)	1.051	0.0119 / 0.0115
	Joint Position (rad)	1.006	/
	Joint Velocity (rad/s)	1.025	/
Physical World (Run)	Forward Velocity (m/s)	0.972	0.1894 / 0.1908
	Body Height (m)	1.021	0.0190 / 0.0186
	Joint Position (rad)	1.009	/
	Joint Velocity (rad/s)	1.037	/

The bold values are the average values of three separate physical experiments.

that RD-WBC outperforms FD-WBC in this aspect. However, it is unclear whether this discrepancy arises from the deviation in the experimental environment or the absence of high real-time performance for the FD-WBC method. Evaluating position and velocity tracking errors in the joint space provides more meaningful insights. Notably, regardless of whether the test involves fast walking or running, the RMSE ratio for the ankle joint trajectory ($q_{\text{pitch}}, \dot{q}_{\text{pitch}}$) remains close to 1.

To illustrate the differences in CPU consumption between RD-WBC and FD-WBC, we compare the average computation times for solving the QP problems across different contact phases (CP), as well as the average time required to calculate the Jacobian derivative terms (JDT) on the right-hand side of (6), which are omitted in RD-WBC. Table V summarizes the sizes of the optimization variables (n_p) and the closed-loop constraints (n_c) before and after simplification. RD-WBC reduces the number of optimization variables by 16 and eliminates 12 equality constraints, leading to over a 20% reduction in average computation time compared to FD-WBC. Notably, the time required to calculate JDT is negligible compared to the time required for solving the QP problem, emphasizing that the improved

TABLE V
COMPARISON OF QP SIZES AND CPU TIME BETWEEN [17] AND OURS

Method	CP	QP Size	JDT Time	QP Time	Speedup
		n_q	n_c	$t_{\text{JDT}} (\mu\text{s})$	$\frac{t - t}{t} \%$
FD-WBC [17]	DS	78	12	1.621	0.645
	LS/RS	62	12	1.423	0.490
	NS	46	—	0.977	—
RD-WBC	DS	62	0	0.473	26.66
	LS/RS	46	0	0.376	23.27
	NS	30	—	0.225	24.50

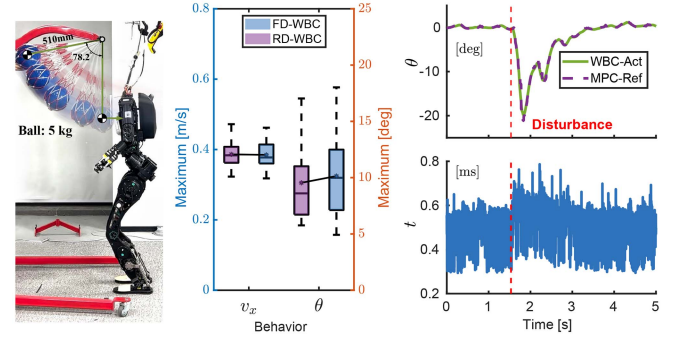


Fig. 9. Performance evaluation of the robot's body pitch angle θ , forward speed v_x , and the computational time t of QP in the disturbance tests.

computational efficiency mainly stems from simplifying the QP problem.

4) *Disturbance Rejection Capability*: We conduct an external force disturbance test to demonstrate the effect of the simplified model on the robot's behaviors during disturbances. A 5 kg ball is released from a fixed height shown in Fig. 9 (left), and the experiment is repeated 20 times for both RD-WBC and FD-WBC.

Fig. 9 (middle) illustrates the distribution of the maximum body forward velocity and the maximum body pitch angle over 20 disturbance tests. Despite comparable fluctuations in the speed during the disturbances, indicating similar levels of impact, RD-WBC exhibits a smaller deviation in the body pitch angle than FD-WBC. This result can be further explained in Fig. 9 (right). When the robot encounters a severe impact causing a sudden state change, the computation time for FD-WBC may increase, potentially affecting its real-time control performance.

C. Discussion

The improvement of our control architecture, as outlined in Table V, is achieved by neglecting the closed-loop acceleration constraints, thereby reducing the number of optimization variables and constraints in the QP problem. This trade-off, where the minor motion tracking error is sacrificed for enhanced computational efficiency, is justified and beneficial in many scenarios. Specifically, our approach is well-suited for robots such as CogIMon [6], Kangaroo [17], and Digit [18], where the connecting rods of the PM contribute minimally to the overall dynamics compared to other links [18]. In these cases, RD-WBC effectively handles the tasks without significant accuracy loss, providing notable benefits for real-time applications, as demonstrated by the dynamic locomotion and disturbance rejection test results.

The rationale behind our assumption is explained in Section V-B1. RD-WBC functions primarily during the support phase but may introduce slight errors during the swing phase. To further enhance the implementation of RD-WBC, researchers can apply the method outlined in that section to evaluate model errors specific to their robots. If the NTPE metric deviates significantly from the results in Table III, the risk of assumption failure may increase. Notably, appropriate joint PD torque compensation during the swing phase can effectively mitigate this risk. Furthermore, RD-WBC is limited in scenarios that require actuated joint acceleration constraints, but actuated torque constraints can still be utilized as an alternative to prevent hardware failures.

VI. CONCLUSION AND FUTURE WORK

This letter presents a reduced-dimensional whole-body controller based on a model simplification strategy tailored for series-parallel bipedal robots. To address the high complexity of the complete model introduced by PM, we propose neglecting the closed-loop acceleration constraints in the QP optimization. Physical experiment results demonstrate that accounting for the inertial forces due to the parallel joint acceleration, at the cost of significantly increased computational burden, is not justified. By sacrificing a lightweight model accuracy, we achieve over a 20% improvement in computational efficiency without compromising dynamic locomotion performance and disturbance rejection capability.

In the future, we plan to implement our approach on series-parallel robots equipped with linear actuators [3], which have more additional parallel joints and kinematic loops. We will explore the applicability and effectiveness of RD-WBC across robots with different drive types.

REFERENCES

- [1] V. Klemm et al., “LQR-Assisted whole-body control of a wheeled bipedal robot with kinematic loops,” *IEEE Robot. Automat. Lett.*, vol. 5, no. 2, pp. 3745–3752, Apr. 2020.
- [2] J. Englsberger et al., “Overview of the torque-controlled humanoid robot TORO,” in *Proc. IEEE-RAS 14th Int. Conf. Humanoid Robots*, 2014, pp. 916–923.
- [3] J. Eber et al., “Design, analysis and control of the series-parallel hybrid RH5 humanoid robot,” in *Proc. IEEE-RAS 20th Int. Conf. Humanoid Robots*, 2021, pp. 400–407.
- [4] A. Roig et al., “On the hardware design and control architecture of the humanoid robot kangaroo,” in *Proc. 6th Workshop Legged Robots during Int. Conf. Robot. Autom.*, May 2022.
- [5] D. Mronga, S. Kumar, and F. Kirchner, “Whole-body control of series-parallel hybrid robots,” in *Proc. IEEE Int. Conf. Robot. Automat.*, 2022, pp. 228–234.
- [6] C. Zhou and N. Tsagarakis, “On the comprehensive kinematics analysis of a humanoid parallel ankle mechanism,” *J. Mechanisms Robot.*, vol. 10, no. 5, Oct. 2018, Art. no. 051015.
- [7] D. Kim et al., “Dynamic locomotion for passive-ankle biped robots and humanoids using whole-body locomotion control,” *Int. J. Robot. Res.*, vol. 39, no. 8, pp. 936–956, Jul. 2020.
- [8] D. Kim et al., “Highly dynamic quadruped locomotion via whole-body impulse control and model predictive control,” Sep. 2019, *arXiv:1909.06586*.
- [9] M. Bjelonic et al., “Keep rollin’—whole-body motion control and planning for wheeled quadrupedal robots,” *IEEE Robot. Automat. Lett.*, vol. 4, no. 2, pp. 2116–2123, Apr. 2019.
- [10] S. Kajita et al., “Resolved momentum control: Humanoid motion planning based on the linear and angular momentum,” in *Proc. IEEE/RSJ Int. Conf. Intell. Robots Syst.*, 2003, pp. 1644–1650.
- [11] N. Mansard, O. Khatib, and A. Kheddar, “A unified approach to integrate unilateral constraints in the stack of tasks,” *IEEE Trans. Robot.*, vol. 25, no. 3, pp. 670–685, Jun. 2009.
- [12] M. Mistry and L. Righetti, “Operational space control of constrained and underactuated systems,” in *Proc. Robot. Sci. Syst.*, 2011, Art. no. 225.
- [13] A. Escande et al., “Hierarchical quadratic programming: Fast online humanoid-robot motion generation,” *Int. J. Robot. Res.*, vol. 33, no. 7, pp. 1006–1028, Jun. 2014.
- [14] D. Kim, J. Lee, J. Ahn, O. Campbell, H. Hwang, and L. Sentis, “Computationally-robust and efficient prioritized whole-body controller with contact constraints,” in *Proc. IEEE/RSJ Int. Conf. Intell. Robots Syst.*, 2018, pp. 1–8.
- [15] K. Bouyarmane, K. Chappellet, J. Vaillant, and A. Kheddar, “Quadratic programming for multirobot and task-space force control,” *IEEE Trans. Robot.*, vol. 35, no. 1, pp. 64–77, Feb. 2019.
- [16] M. A. Hopkins, D. W. Hong, and A. Leonessa, “Compliant locomotion using whole-body control and divergent component of motion tracking,” in *Proc. IEEE Int. Conf. Robot. Automat.*, 2015, pp. 5726–5733.
- [17] S. Sovukluk, J. Englsberger, and C. Ott, “Whole body control formulation for humanoid robots with closed/parallel kinematic chains: Kangaroo case study,” in *Proc. IEEE/RSJ Int. Conf. Intell. Robots Syst.*, 2023, pp. 10390–10396.
- [18] V. C. Paredes and A. Hereid, “Safe whole-body task space control for humanoid robots,” in *Proc. 2024 Amer. Control Conf.*, 2024, pp. 949–956.
- [19] R. Featherstone, *Rigid Body Dynamics Algorithms*. Berlin, Germany: Springer, 2008.
- [20] S. Sovukluk, J. Englsberger, and C. Ott, “Highly maneuverable humanoid running via 3D SLIP foot dynamics,” *IEEE Robot. Automat. Lett.*, vol. 9, no. 2, pp. 1131–1138, Feb. 2024.
- [21] T.-S. Nguyen et al., “Motion control algorithms based on the dynamic modelling of kinematically redundant hybrid parallel robots,” *Mechatronics*, vol. 76, Jun. 2021, Art. no. 102555.
- [22] N. Edoimoya and C. E. Okwudire, “A generalized and efficient control-oriented modeling approach for vibration-prone delta 3D printers using receptance coupling,” *IEEE Trans. Automat. Sci. Eng.*, vol. 20, no. 3, pp. 1539–1550, Jul. 2023.
- [23] S. Kumar, J. Martensen, A. Mueller, and F. Kirchner, “Model simplification for dynamic control of series-parallel hybrid robots - a representative study on the effects of neglected dynamics shivesh,” in *Proc. IEEE/RSJ Int. Conf. Intell. Robots Syst.*, 2019, pp. 5701–5708.
- [24] J. M. Escorcia-Hernandez, A. Chemori, and H. Aguilar-Sierra, “Adaptive RISE feedback control for robotized machining with PKMs: Design and real-time experiments,” *IEEE Trans. Control Syst. Technol.*, vol. 31, no. 1, pp. 39–54, Jan. 2023.
- [25] X. Xiong and A. D. Ames, “Bipedal hopping: Reduced-order model embedding via optimization-based control,” in *Proc. IEEE/RSJ Int. Conf. Intell. Robots Syst.*, 2018, pp. 3821–3828.
- [26] C. Dario Bellicoso, C. Gehring, J. Hwangbo, P. Fankhauser, and M. Hutter, “Perception-less terrain adaptation through whole body control and hierarchical optimization,” in *Proc. IEEE-RAS 16th Int. Conf. Humanoid Robots*, 2016, pp. 558–564.
- [27] J.-P. Sleiman, F. Farshidian, M. V. Minniti, and M. Hutter, “A unified MPC framework for whole-body dynamic locomotion and manipulation,” *IEEE Robot. Automat. Lett.*, vol. 6, no. 3, pp. 4688–4695, Jul. 2021.
- [28] A. Herzog et al., “Momentum control with hierarchical inverse dynamics on a torque-controlled humanoid,” *Auton. Robots*, vol. 40, no. 3, pp. 473–491, Mar. 2016.
- [29] E. Todorov, T. Erez, and Y. Tassa, “MuJoCo: A physics engine for model-based control,” in *Proc. IEEE/RSJ Int. Conf. Intell. Robots Syst.*, 2012, pp. 5026–5033.
- [30] G. Guennebaud, “Eigen v3,” 2011. [Online]. Available: <http://eigen.tuxfamily.org>
- [31] J. Carpentier et al., “The pinocchio C++ library : A fast and flexible implementation of rigid body dynamics algorithms and their analytical derivatives,” in *Proc. IEEE/SICE Int. Symp. Syst. Integration*, 2019, pp. 614–619.
- [32] H. J. Ferreau et al., “qpOASES: A parametric active-set algorithm for quadratic programming,” *Math. Program. Comput.*, vol. 6, no. 4, pp. 327–363, Dec. 2014.
- [33] M. Bloesch et al., “State estimation for legged robots: Consistent fusion of leg kinematics and IMU,” in *Proc. Conf. Robot.*, 2013, pp. 17–24.